# Experimental and Theoretical Study on the Nature of Adsorbed Oxygen Species on Shaped Ceria Nanoparticles

*Christian Schilling[a], M. Verónica Ganduglia-Pirovano*[b], and Christian Hess*[a]*

[a] Eduard-Zintl-Institut für Anorganische und Physikalische Chemie, Technische Universität Darmstadt, Alarich-Weiss-Str. 8, 64287 Darmstadt, Germany

[b] Instituto de Catálisis y Petroleoquímica, Consejo Superior de Investigaciones Científicas, Marie Curie 2, 28049, Madrid, Spain

## Supporting Information

# 1. Experimental details

## Synthesis

Ceria sheets were obtained from decomposition of $Ce(NO_3)_3 \cdot 6H_2O$ at 600°C in an electric oven after employing a ramp of 6°C/min and then keeping the temperature at 600°C for 12h. This protocol was applied twice. No residual nitrate impurities can be detected by Raman spectroscopy. [1]

Ceria polyhedra and cubes were synthesized according to Mai et al. [2] For the polyhedra 1.946 g $Ce(NO_3)_3 \cdot 6H_2O$ were dissolved in 11 ml deionized water and added to 79 ml of 0.011 ML NaOH solution (Grüssing GmbH, 98%) and after stirring for 30 minutes the suspension was transferred into a homemade Teflon autoclave (volume 140 ml) and heated in an electric oven to 180°C using a ramp of 1°C/min and keeping the temperature at 180°C for 18h.

Ceria cubes were synthesized in a similar fashion 22.5g NaOH were dissolved in 79 ml deionized water and added to the $Ce(NO_3)_3 \cdot 6H_2O$ suspension. The oven was heated again to 180°C using the same ramp as for polyhedral.

After the synthesis of the ceria nanoparticles as described above, no further treatment was applied.

## In situ Raman

The in situ Raman setup was described in previously. [3 4] Briefly, an in situ cell of 50 ml was attached to a X-ray photoelectron spectrometer. For Raman measurements a fiber optic was applied to the cell allowing for measurements without passing a window. For laser excitation, a frequency doubled Nd:YAG laser (Cobolt) was employed ($\lambda$ = 532 nm). The laser power at the sample was adjusted to 1 mW. Raman spectra were recorded on a HL5R transmission spectrometer (Kaiser Optical) with a resolution of 5 $cm^{-1}$, whereas the band stability is better than 0.3 $cm^{-1}$. The spectra are the sum of 5 accumulations with a single exposure time of 40s.

The sample (25-30 mg) was placed in a stainless steel sample holder with 8mm in diameter and 0.5 mm in depth. For in situ measurements, a gas flow of 25% $O_2$ in Ar (100 ml/min total flow rate) was applied to the cell. The sample was heated by an electric heating and the sample temperature was monitored by a thermocouple in direct contact with the sample.

During the temperature-dependent experiments the samples were first heated to the respective temperature in 25% $O_2$/Ar flow by applying a heating ramp of 15°C/min and then held at each of those temperatures for about 60 min. Cooling from 120°C back to 21°C was not actively controlled but took place initially at 15°C/min and later at 5°C/min on average.

All spectra exhibit the ceria 2LO overtone at 1170 $cm^{-1}$ that is considered to remain stable in intensity and can therefore be used as an internal reference for quantitative intensity analysis of adsorbed species.

**TEM**

Transmission electron microscopy (TEM) characterization was performed at a JEOL JEM-2100F (Tokyo, Japan) equipped with a Schottky field emitter operating at a nominal acceleration voltage of 200 kV. A small amount of powder was dispersed in ethanol by ultrasound treatment (Bandelin) for 30s. A droplet of the dispersion was applied to a holey carbon grid (Plano) and allowed to dry. To avoid charging under the electron beam, the grid was coated with carbon (Baltec MED010).

For the evaluation of the particle size, the largest and smallest observed particles were measured and reported in Table S1.

**BET**

$N_2$ adsorption was conducted on a SURFER (ThermoFisher Scientific). Prior to the adsorption experiments, the sample was outgassed at 65°C in high vacuum for 24h. For determination of the specific surface area the $N_2$ adsorption curve was fitted to a BET model. [5]

**Table S1:** Characteristics of the synthesized ceria nanostructures: specific surface areas as determined from $N_2$ adsorption experiments employing the BET model, crystal sizes as derived from the specific surface areas and as determined from TEM images, TEM layer spacings, as well as the determined surface terminations.

| Nanostructure | Specific surface area (BET) [$m^2/g$] | Crystal size [a] (BET) [nm] | Crystal size (TEM) [nm] | Layer spacing [nm] | Surface facet |
|---|---|---|---|---|---|
| Sheets | 61 | 13.5 | 12 | 0.31 | $CeO_2$(111) |
| Polyhedra | 124 | 6.6 | 6-10 | 0.31 | $CeO_2$(111) |
| Cubes | 51 | 16.2 | 11-60 | 0.27 | $CeO_2$(100) |

[a] The crystal size is derived from the specific surface area (BET model) assuming spherical particles for sheets and polyhedral and cubic particles for cubes.

## 2. In situ Raman spectra

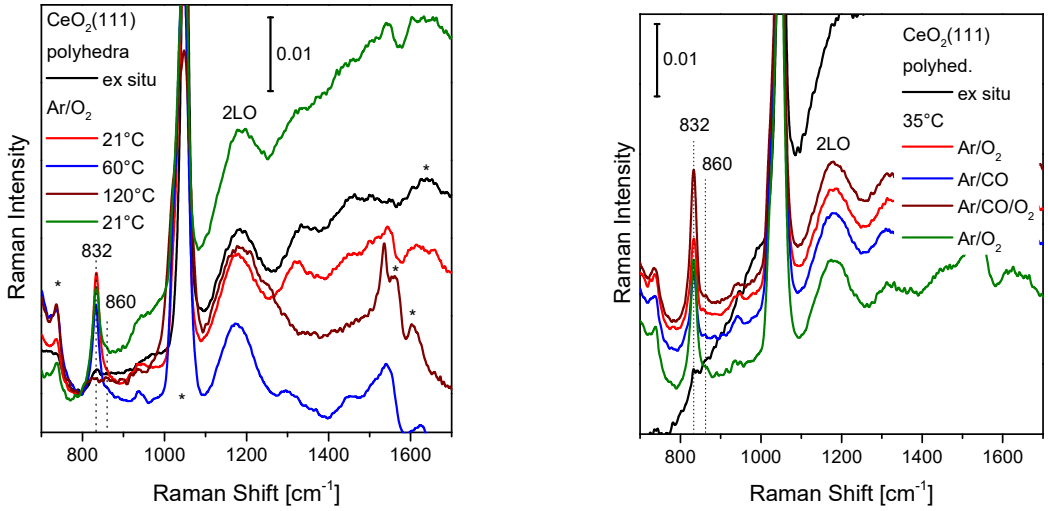


**Figure S1:** In situ Raman spectra of ceria polyhedra showing the spectral region of the O–O stretching vibrations of adsorbed molecular oxygen ($O_2^{\delta-}$), superoxide ($O_2^-$) and peroxide ($O_2^{2-}$) species. The corresponding spectra of sheets and cubes are shown in Fig. 2 (main text). The polyhedra exhibit nitrate impurities (bands at 735 $cm^{-1}$ and 1040 $cm^{-1}$) as a resulting from the synthesis. [6]

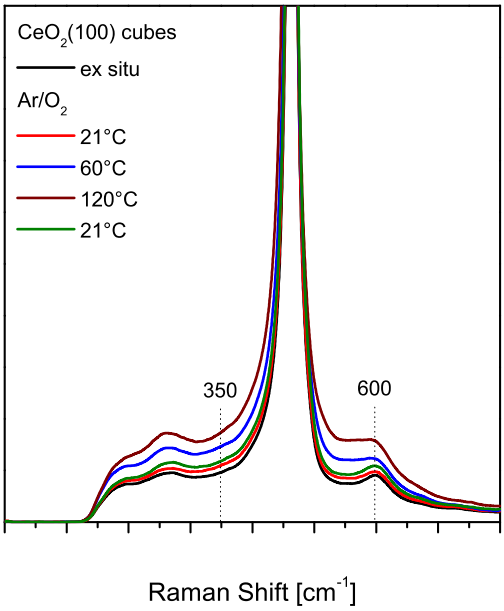


**Figure S2:** In situ Raman spectra of ceria cubes at room temperature, 60°C, 120°C, and room temperature again. The spectrum after treatment at 120°C (green) is identical to the spectrum before temperature treatment (red) and no band at 246 $cm^{-1}$ is observed that is characteristic of the $CeO_2$(111) facet. Therefore, we conclude that the $CeO_2$(100) facet is stable up to 120°C.

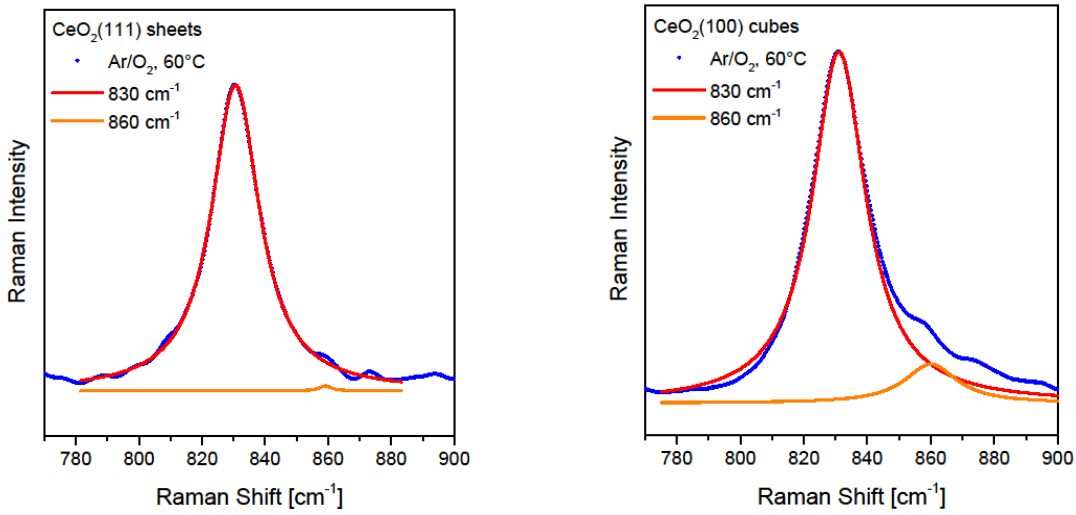


**Figure S3:** In situ Raman spectra of ceria sheets and cubes at 60°C in $Ar/O_2$ flow together with the results of a least-square fit analysis showing the contributions of peroxide species at 830 and 860 $cm^{-1}$.

## 3. DFT calculations

### 3.a. Computational details

The bulk lattice constant of fluorite type $CeO_2$ ($Fm\bar{3}m$) was calculated for the primitive cell containing one formula unit ($CeO_2$) as $a_0$ = 5.484 Å. [7] We applied spin-polarized DFT in the DFT+U approach [8] with the generalized gradient corrected approximation (GGA) by Perdew, Burke and Ernzerhof (PBE) [9] as implemented in the Vienna ab initio simulation package (VASP, version 5.3.5, http://www. vasp.at/). [10-14] The $U_{eff}$ value of 4.5 eV [15] was used for the Ce 4f states. The Kohn−Sham equations were solved employing the projected augmented wave (PAW) method. [16] The Ce (5s, 5p, 6s, 4f, 5d) and O (2s, 2p) valence electrons were treated with a plane wave cutoff of 400 eV.

The $CeO_2$(111) surface was modeled using a supercell containing a 3 O−Ce−O trilayers (TL) slab with calculated $CeO_2$ bulk equilibrium lattice constant. The $CeO_2$(100) surface was modeled by 7 to 15 atomic layers; 11 atomic layers are sufficient to reach convergence of the surface energy for a checkerboard type arrangement of the surface oxygen ions (see below). A vacuum layer of more than 10 Å was added to the slabs to avoid interaction between surfaces of consecutive slabs.

Chemisorbed superoxide ($O_2^-$) species were modeled on the $CeO_{2-x}$(111) surface [$O_2^-/CeO_{2-x}$(111)] with (2×2) surface periodicity and a (3×3×1) Monkhorst-Pack grid. [17] Peroxide ($O_2^{2-}$) and superoxide ($O_2^-$) formation was also considered at the $CeO_{2-x}$(100) surface [$O_2^{2-}/CeO_{2-x}$(100), $O_2^-/CeO_{2-x}$(100)] using a 11 layer thick slab with *c*(1×1), *p*(2×2) and *c*(2×2) surface periodicities with (4×4×1), (3×3×1) and (2×2×1) Monkhorst-Pack grids, respectively. All surfaces were allowed to relax with the bottom O−Ce−O trilayer of the $CeO_2$(111) and $CeO_2$(100) slabs as well as the surface unit cell kept fixed during geometry optimization until residual forces were reduced to 0.01 eV/Å, with a total energy precision of $10^{-6}$ eV.

Selected calculations were repeated to account for dispersion (van der Waals) interactions. The approach of Grimme [18 19] was employed with semi empirical parameters. A global scaling factor $s_6$ = 0.75 was used, $C_6$ and $R_0$ are defined for each atom, i.e., $C_6$: 20.0, 0.70, 21.23, 1.75 J nm$^6$ mol$^{-1}$, and $R_0$: 1.860, 1.342, 1.772, 1.452 Å for Ce, O, Au and C, respectively. [20] The cutoff radius for dispersive interactions to be taken into account was set to 30 Å.

In order to calculate the mass-weighted Hessian matrix required for vibrational frequency calculations in the harmonic approximation, the force-constants were computed either from numerical differentiation using the finite difference approach with ±0.015 Å displacements, or from a density functional perturbation (or linear response) theory (DFPT) [21] technique, both implemented in the VASP package. [22] The latter is not available when van der Waals / dispersion interactions are included, and thus it was used with PBE+U only. To evaluate the normal mode position with a finite differences approach with PBE+U including dispersion interaction a tight self-consistent field (SCF) energy convergence criterion of $10^{-8}$ eV was used. Once the normal modes are calculated, it is possible to model their associated Raman activity as follows: employing the VASP code and with the PBE+U functional, Born effective charges and the macroscopic dielectric tensor can be computed using DFPT. Raman scattering activity requires computing the change in the macroscopic dielectric tensor with respect to each normal mode, and thus relates to the third derivative of the energy with respect to atomic positions. [23] In practice, the dielectric matrix is calculated for two structures where the atoms are displaced by +0.005 Å and −0.005 Å along each normal mode vector, respectively, and derivatives are obtained with a finite differences approach (see Supporting Information of reference [7]).

In general, the observed facilitated adsorption of dioxygen species at (100) facets as compared to the (111) ones is in-line with the calculated adsorption energies. The surface oxygen vacancy formation energy is lowered for the (100) facet ($E_{\mathrm{vac,O}} = 1.824$ eV for a structure with $p(2\times2)$ periodicity at 0.25 ML, Table S4) compared to the (111) facet ($E_{\mathrm{vac,O}} = 2.265$ eV for a structure with (2×2) periodicity at 0.25 ML, Table S2). However, the adsorption energy for a peroxide at the $CeO_{2-x}$(100) facet ($E_{\mathrm{ads},O_2^{2-}} = -2.141$ eV) is increase compared to the $CeO_{2-x}$(111) facet ($E_{\mathrm{ads},O_2^{2-}} = -1.900$ eV). The same behavior holds true for the most stable superoxide configurations at the (100) facet ($E_{\mathrm{ads},O_2^{-}} = -1.625$ eV, $p(2\times2)$ with NN $Ce^{3+}$, Table S4) and the (111) facet ($E_{\mathrm{ads},O_2^{-}} = -1.422$ eV (2×2) with NNN $Ce^{3+}$, Table S2). For direct comparison the difference between $E_{\mathrm{ads},O_2^{x-}}$ and $E_{\mathrm{vac,O}}$, i.e., the net formation energy for an adsorbed oxygen species, hereinafter referred to as $E_{\mathrm{ads,O}}$, was calculated for all structures and visualized for peroxide and superoxide formation at the (100) facet in Figs. S11 and S12.

### 3.b. Results $CeO_2(111)$

Peroxide adsorption on the $CeO_2(111)$ surface and corresponding vibrational frequency analysis is reported in reference [7].

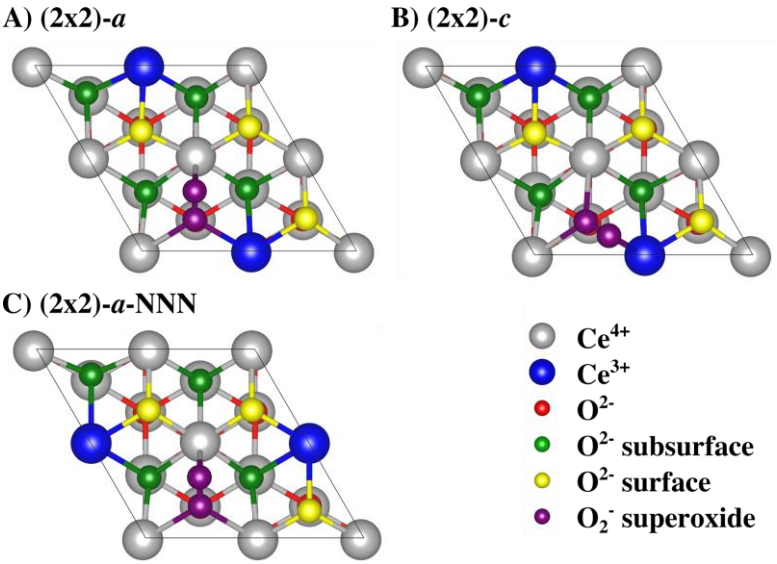


**Figure S4:** Top view of the $O_2^-/CeO_{2-x}(111)$ surface with (2×2) periodicity, $O_{vac}$ = 1 (0.25 ML coverage) and different locations for the $Ce^{3+}$, (A) and (B) NN $Ce^{3+}$, and C) NNN $Ce^{3+}$. Here and in the following gray and blue balls indicate $Ce^{4+}$ and $Ce^{3+}$, red balls indicate bulk oxygen ($O^{2-}$), green balls subsurface and yellow balls surface oxygen, respectively. Superoxide species are shown in purple.

**Table S2:** Total energy $E_{\mathrm{tot}}$ and surface oxygen vacancy formation energy $E_{\mathrm{vac,O}}$ $\left[E_{\mathrm{vac,O,}} = E_{\mathrm{CeO_{2-x(111)}}} + \frac{1}{2}E_{\mathrm{O_2}} - E_{\mathrm{CeO_2(111)}}\right]$ for the $CeO_2$(111) surface with (2×2) periodicity with respect to $\frac{1}{2}E(\mathrm{O_2}) = 4.939$ eV. Molecular $E_{\mathrm{ads,O_2^{x-}}}$ $(x = 1, 2)$ $\left[E_{\mathrm{ads,O_2^{x-}}} = E_{\mathrm{O_2^{x-}/CeO_{2-x}(111)}} - E_{\mathrm{O_2}} - E_{\mathrm{CeO_{2-x}(111)}}\right]$, and net $E_{\mathrm{ads,O}}$ $\left[E_{\mathrm{ads,O,}} = E_{\mathrm{O_2^{x-}/CeO_{2-x}(111)}} - \frac{1}{2}E_{\mathrm{O_2}} - E_{\mathrm{CeO_2(111)}}\right]$ adsorption energies of peroxides ($O_2^{2-}$) and superoxide ($O_2^-$) species at the $CeO_{2-x}$(111) surface with (2×2) periodicity. Raman shift and Raman intensity for the $O_2^{x-}$ stretching mode and $O_2^{x-}$bond length.

| Structure | Cov. | $E_{\mathrm{tot}}$ [eV] | $E_{\mathrm{vac,O}}$ [eV/$O_{vac}$] | $E_{\mathrm{ads,O_2^{x-}}}$ [eV/$O_2^{x-}$] | $E_{\mathrm{ads,O}}$ [eV/O] | Raman Shift [$cm^{-1}$] | Intensity | Bond length [Å] |
|---|---|---|---|---|---|---|---|---|
| $CeO_2$(111) | | -291.330 | | | | | | |
| $CeO_{2-x}$(111) surf. vac | | -284.125 | 2.265 | | | | | |
| $CeO_{2-x}$(111) subsurface vac. | | -284.499 | 1.892 | | | | | |
| **Peroxide $O_2^{2-}/CeO_{2-x}$(111)** [7] | | | | | | | | |
| (2×2)-*a* | 0.25 | -295.905 | | -1.900 | 0.365 | 900 | 2160 | 1.443 |
| (2×2)-*b* | 0.25 | -295.924 | | -1.919 | 0.345 | 938 | 855 | 1.446 |
| (1×1)-*b* | 1.00 | -77.275 | | -1.773 | 0.497 | 973 | 605 | 1.433 |

| | | | | | | | |
|---|---|---|---|---|---|---|---|
| **Superoxide $O_2^-/CeO_{2-x}$(111)** | | | | | | | |
| (2×2)-*a* | 0.25 | -295.294 | -1.289 | 0.976 | 1134 | 11800 | 1.350 |
| (2×2)-*c* | 0.25 | -295.214 | -1.209 | 1.056 | 1132 | 2900 | 1.351 |
| (2×2)-*a*-NNN | 0.25 | -295.427 | -1.422 | 0.843 | 1134 | 3300 | 1.346 |
| **Molecular $O_2$** | | | | | | | |
| $O_2$ | gas | -9.879 | | | 1561 | | 1.234 |

### 3.c. Results $CeO_2(100)$

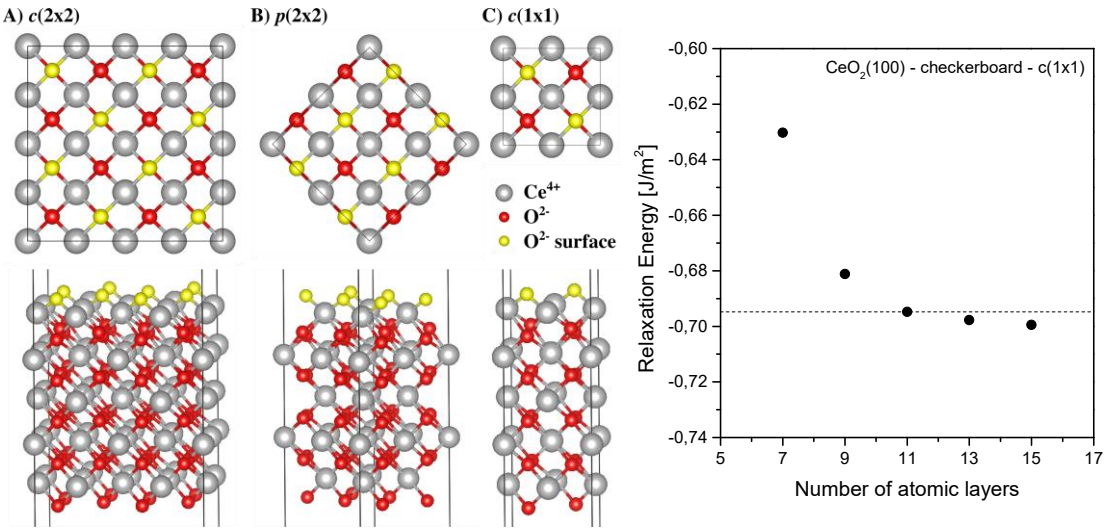


**Figure S5:** Left: Model for the $CeO_2(100)$ surface with a checkerboard termination and 11 atomic layers with *c*(2x2), *p*(2x2) and *c*(1x1) periodicity (cf. Ref. [24]) Right: Convergence test for the slab thickness is performed by plotting relaxation energy vs. slab thickness. The calculated surface energy for a 11-layer slab (1.45 J $m^{-2}$) is in accordance to Ref. [24] (1.44 J $m^{-2}$). For the $CeO_2(100)$ surface, the outermost oxygen atoms are shown in yellow.

To calculate the relaxation energy, we first calculate the surface energy associated to a bulk-truncated slab, $E_{\mathrm{surf,cut}}$:

$$E_{\mathrm{surf,cut}} = \frac{E_{\mathrm{cut}} - (n-1)E_{\mathrm{CeO_2}}}{2A},$$

where $E_{\mathrm{cut}}$ is the total energy of the bulk-truncated slab with *c*(1×1) surface periodicity, $n$ is the number of atomic layers, $E_{\mathrm{CeO_2}}$ is the total energy of the primitive bulk unit cell, and $A$ is the area of the surface unit cell.

The relaxation energy, $E_{\mathrm{surf,relax}}$, is derived from the total energy of the relaxed slab with the bottom three atomic layers fixed, $E_{\mathrm{CeO_2(100)}}$, as

$$E_{\mathrm{surf,relax}} = \frac{E_{\mathrm{CeO_2(100)}} - E_{\mathrm{cut}}}{A}$$

Finally, the surface energy is calculated as the sum of $E_{\mathrm{surf,cut}}$ and $E_{\mathrm{surf,relax}}$, which for a slab consisting of 11 atomic layers with $c(1\times1)$ periodicity amounts to 1.45 J m$^{-2}$.

$$E_{\mathrm{surf}} = E_{\mathrm{surf,cut}} + E_{\mathrm{surf,relax}} = 1.45\ \mathrm{J\ m^{-2}}$$

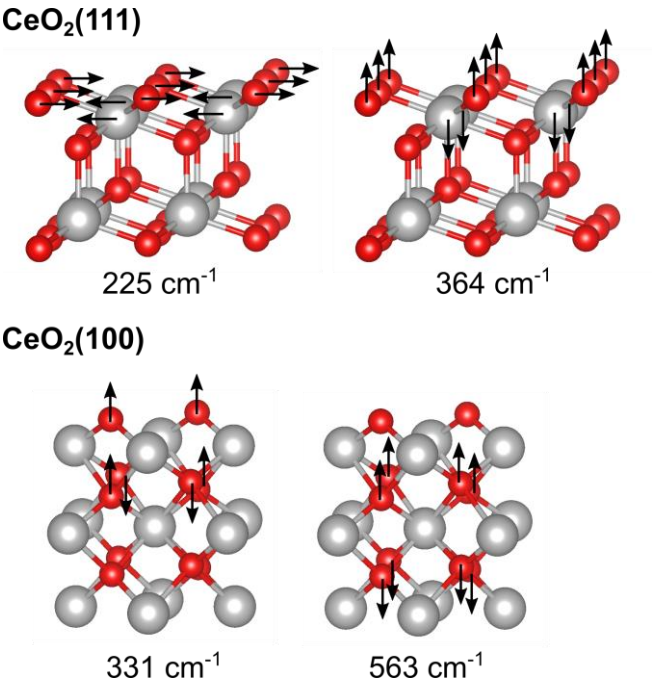


**Figure S6:** Characteristic vibrational modes and frequencies (not scaled) of the $CeO_2(111)$ surface (top) and the $CeO_2(100)$ surface (bottom). For detailed discussion on the modes at the $CeO_2(111)$ surface see reference [7]. At the $CeO_2(100)$ surface, the modes are derived accordingly.

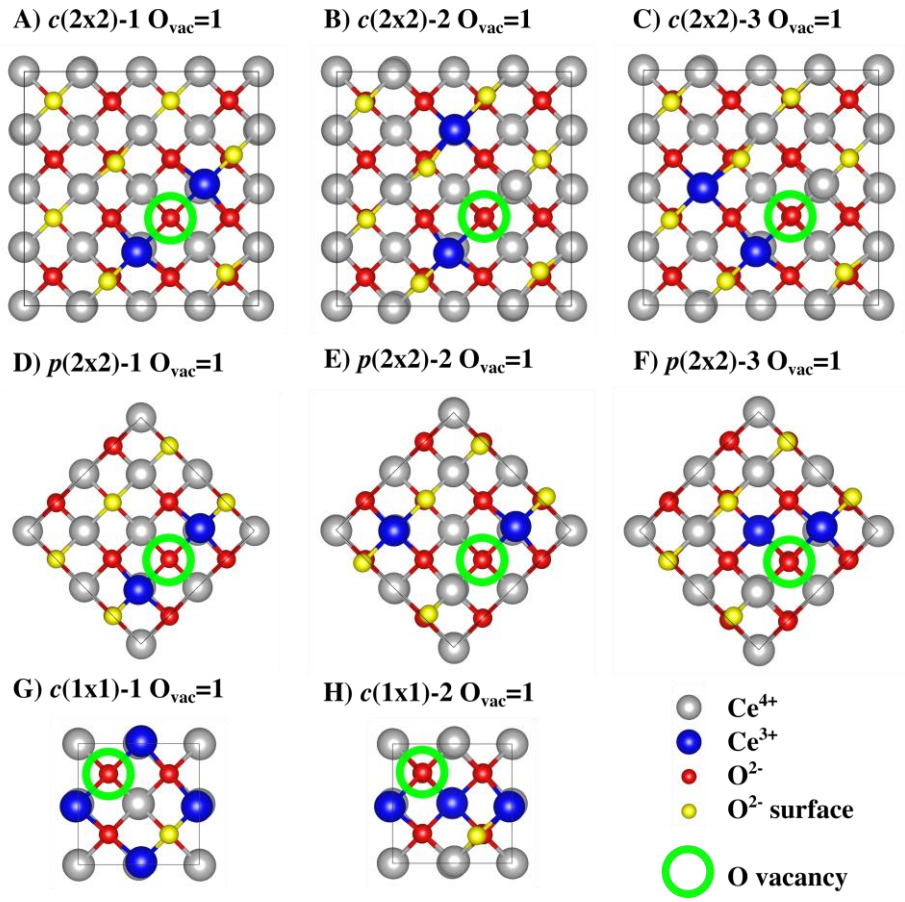


**Figure S7:** Top view of a $CeO_{2-x}(100)$ surface with $O_{vac}$ = 1 and different configurations of the excess charge localization. A-C) *c*(2×2), D-E) *p*(2×2) and G-H) *c*(1×1) periodicity, corresponding to oxygen vacancy concentrations of 0.125, 0.25, and 0.5 ML respectively.

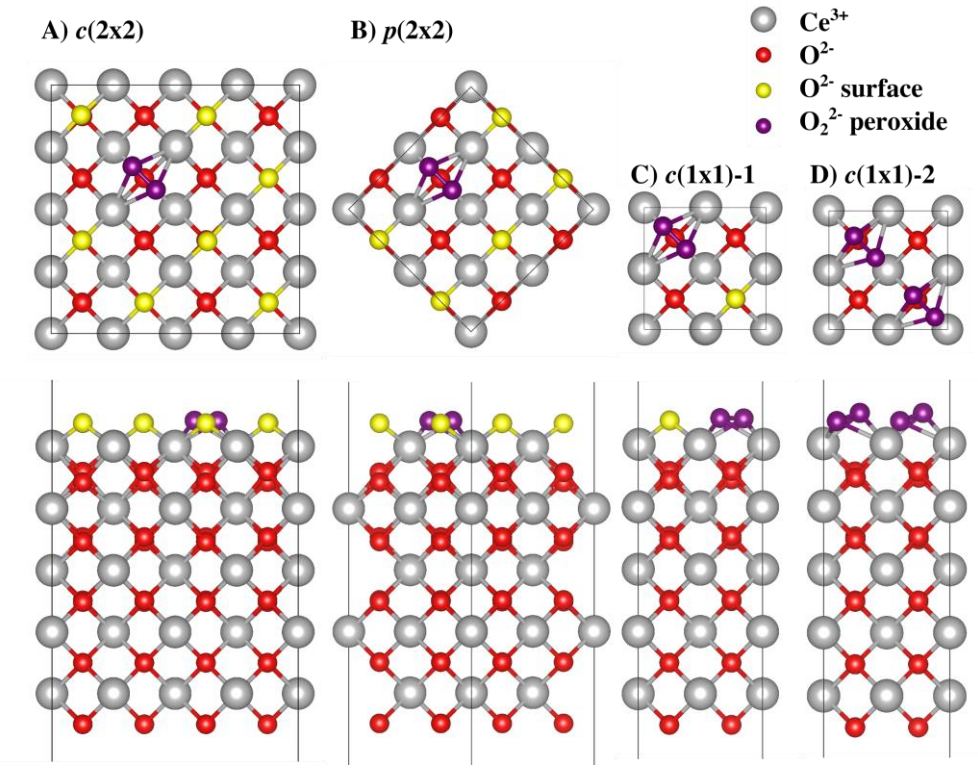


**Figure S8:** Top and side view of peroxide species at the $CeO_{2-x}$(100) surface, $O_2^{2-}/CeO_{2-x}$(100) with A) *c*(2×2) (0.125 ML coverage), B) *p*(2×2) (0.25 ML coverage) and C) *c*(1×1) periodicity (0.5 ML coverage) and D) *c*(1×1) periodicity and 1 ML peroxide coverage.

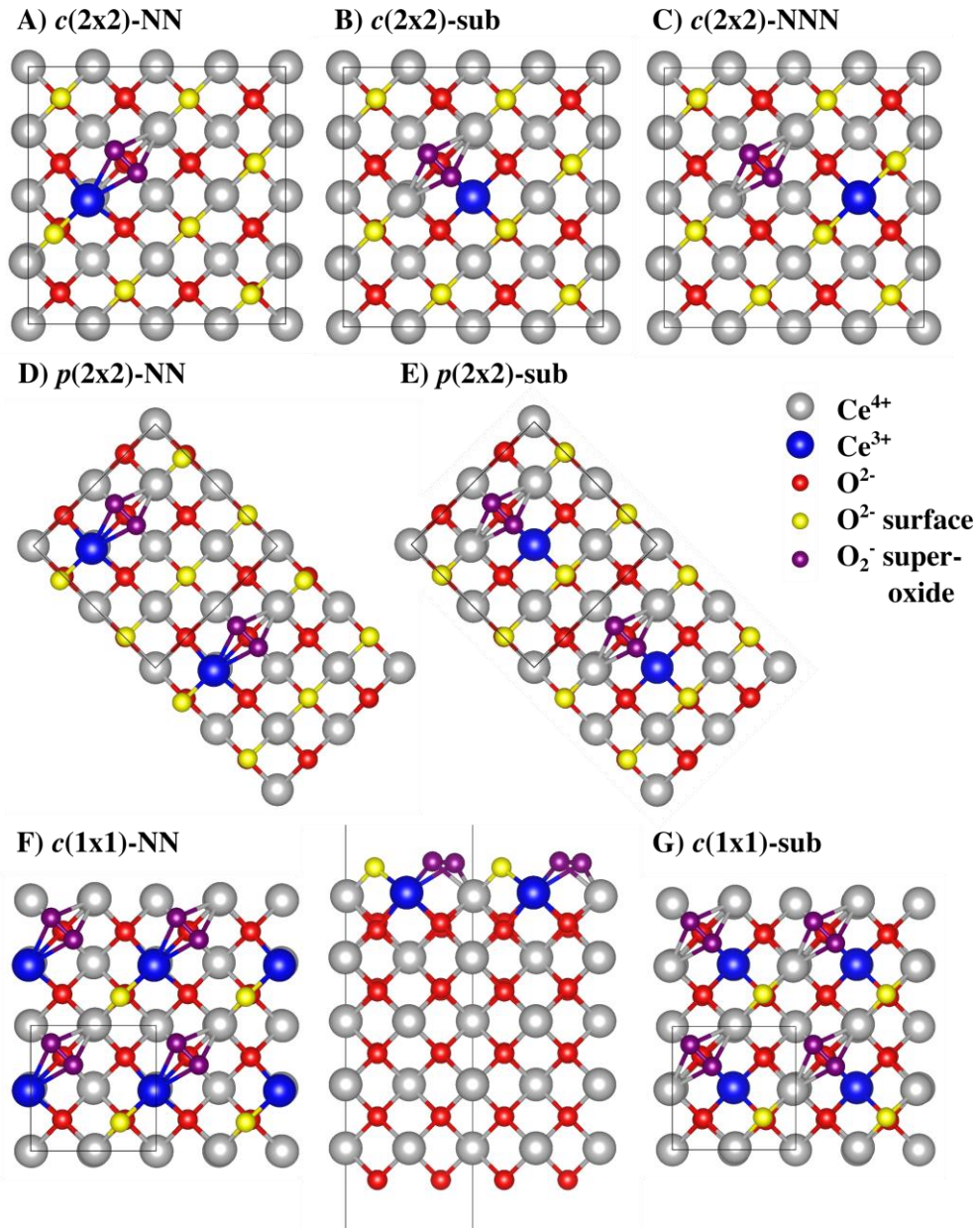


**Figure S9:** Top view of stable superoxide species at the $CeO_{2-x}(100)$ surface, $O_2^-/CeO_{2-x}(100)$ with A-C) $c(2\times2)$, D-E) $p(2\times2)$ and F-G) $c(1\times1)$ periodicity. The excess charge ($Ce^{3+}$) is located in a NN position with respect to the $O_2^-$ species in A), D), and F), in a NNN position in the subsurface in B), E), and G), and in a NNN position at the surface in C). A side view of the $c(1\times1)$-NN configuration shows that the superoxide is indeed flat-lying, i.e., parallel to the surface.

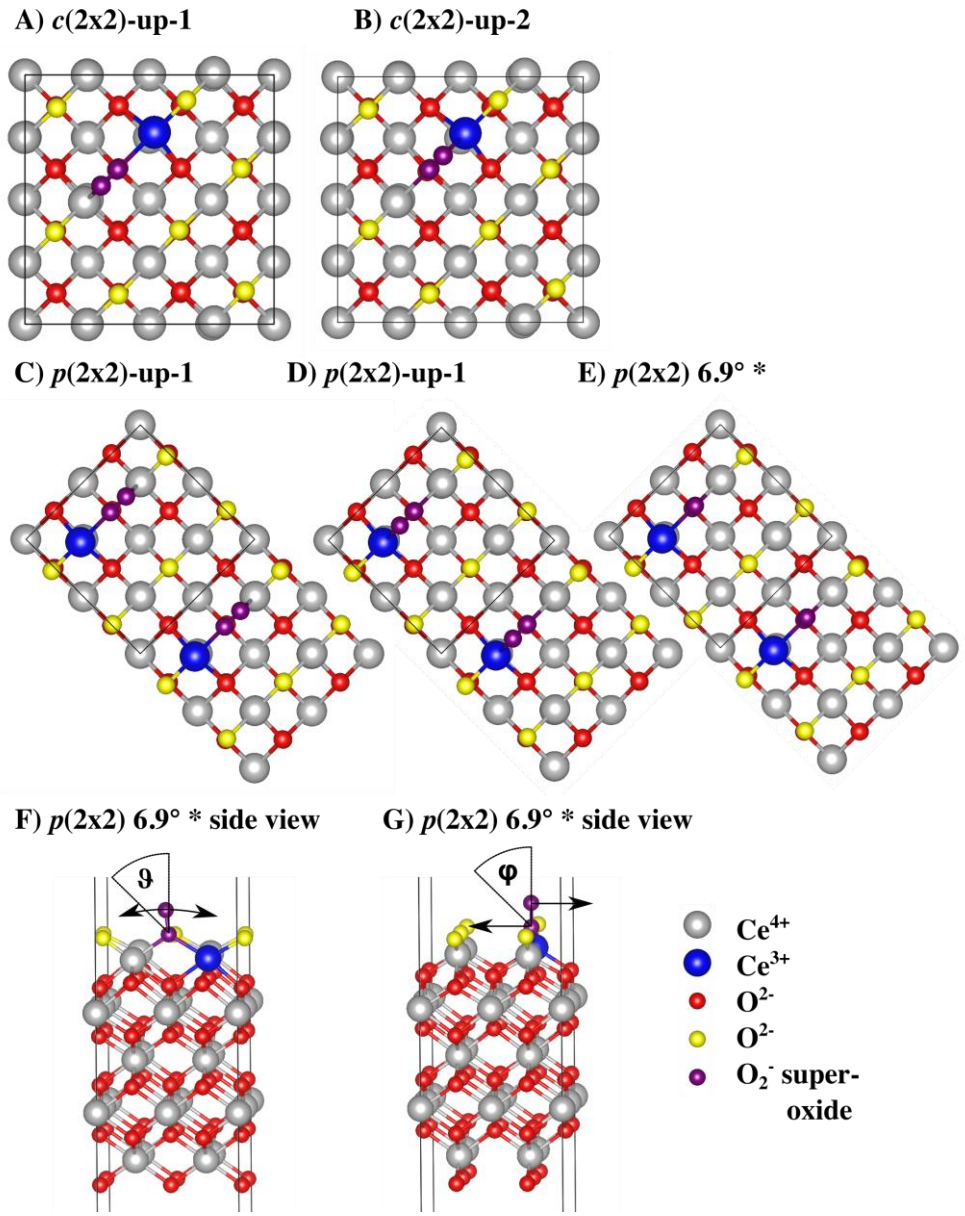


**Figure S10:** Top view of transition state superoxide $O_2^-$ structures (one imaginary frequency) at the $CeO_{2-x}$(100) surface with A-B) *c*(2×2) periodicity C-E) *p*(2×2) periodicity. Structures indicated by up-1 in A) and C) refer to a superoxide molecule tilted towards a NN $Ce^{4+}$ and by up-2 in B) and D) to a superoxide molecule tilted towards a NN $Ce^{3+}$. In the up-1 and up-2 structures, φ=0º, whereas ϑ=53.2º and ϑ=–47.5º, respectively. In E) the superoxide is tilted towards $Ce^{4+}$ with an angle of ϑ=6.9° whereas φ=0º (cf. Ref. [25]). The latter has only been calculated including van der Waals interactions as indicated by an asterisk. For the definition of the angles ϑ and φ see the side views in figures F) and G). The arrows indicate the imaginary frequencies determined for the *p*(2×2) 6.9º * structure (see Table S3).

**Table S3:** Total energy $E_{\mathrm{tot}}$ and oxygen vacancy formation energy $E_{\mathrm{vac,O}}$ for the $CeO_2(100)$ surface with $c(2\times2)$, $p(2\times2)$ and $c(1\times1)$ periodicity with respect to $\frac{1}{2}E(O_2) = 4.933$ eV including van der Waals interactions. Molecular, $E_{\mathrm{ads},O_2^{x-}}$ $(x = 1, 2)$, and net, $E_{\mathrm{ads,O}}$, adsorption energies of peroxide ($O_2^{2-}$) and superoxide ($O_2^{-}$) species at the $CeO_{2-x}(100)$ surface (see Table S2 for definition of $E_{\mathrm{ads},O_2^{x-}}$ and $E_{\mathrm{ads,O}}$). Raman shift and Raman intensity for the $O_2^{x-}$ stretching mode and $O_2^{x-}$ bond length. *Calculations at 600 eV cutoff; the results resemble those in the literature concerning $E_{\mathrm{vac,O}}$ for the $p(2\times2)$-3 $O_{vac} = 1$ structure as well as $E_{\mathrm{ads},O_2^{2-}}$ and the $O_2^{2-}$ vibrational frequency for the $p(2\times2)$ flat structure. [25]

| Structure | Cov. | $E_{\mathrm{tot}}$ [eV] | $E_{\mathrm{vac,O}}$ [eV/$O_{vac}$] | $E_{\mathrm{ads},O_2^{x-}}$ [eV/ $O_2^{x-}$] | $E_{\mathrm{ads,O}}$ [eV/O] | Raman Shift [$cm^{-1}$] | Intensity | Bond length [Å] |
|---|---|---|---|---|---|---|---|---|
| $p(2\times2)$ $O_{vac} = 0$ | | -487.197 | | | | | | |
| $p(2\times2)$ $O_{vac} = 1$ * | | -486.557 | | | | | | |
| $p(2\times2)$-3 $O_{vac} = 1$ | | -480.336 | 1.928 | | | | | |
| $p(2\times2)$-3 $O_{vac} = 1$ * | | -479.711 | 1.901 | | | | | |
| $c(1\times1)$ $O_{vac} = 0$ | | -243.596 | | | | | | |
| $c(1\times1)$ $O_{vac} = 1$ | | -236.529 | 2.134 | | | | | |
| **Peroxide $O_2^{2-}/CeO_{2-x}(100)$** | | | | | | | | |
| $p(2\times2)$ flat | 0.25 | -492.540 | | -2.338 | -0.410 | 868 | - | 1.470 |
| $p(2\times2)$ flat * | 0.25 | -491.893 | | -2.282 | -0.403 | 857.2 | - | 1.472 |
| $c(1\times1)$-1 | 0.5 | -248.945 | | -2.550 | -0.410 | 870 | - | 1.469 |
| $c(1\times1)$-2 | 1 | -253.951 | | - | -0.238 | 908 | - | 1.455 |

| | | | | | | | |
|---|---|---|---|---|---|---|---|
| **Superoxide $O_2^-/CeO_{2-x}$(100)** | | | | | | | |
| *p*(2×2) flat NN | 0.25 | -491.997 | -1.795 | 0.133 | 1043 | - | 1.373 |
| *p*(2×2) flat sub | 0.25 | -491.742 | -1.540 | 0.387 | 1026 | - | 1.384 |
| *p*(2×2) up-1 [a] | 0.25 | -491.538 | -1.338 | 0.592 | 1192 | - | 1.338 |
| *p*(2×2) up-2 [a] | 0.25 | -491.562 | -1.360 | 0.567 | 1189 | - | 1.338 |
| *p*(2×2) 6.9° * [b] | 0.25 | -490.713 | -1.112 | 0.778 | 1125 | - | 1.342 |
| **Molecular $O_2$** | | | | | | | |
| $O_2$ | gas | -9.866 | | | 1563 | - | 1.235 |
| $O_2$ * | gas | -9.890 | | | | | 1.233 |

[a] one imaginary frequency

[b] two imaginary frequencies at 56 $cm^{-1}$ corresponding to a vibration of the outer oxygen atom in direction of $+\vartheta$ and $-\vartheta$ (towards NN $Ce^{4+/3+}$) and at 58 $cm^{-1}$ corresponding to a vibration of the outer oxygen in direction of $-\varphi$, and the inner oxygen in the opposite direction (cf. Fig. S9).

**Table S4:** Total energy $E_{\mathrm{tot}}$ and surface oxygen vacancy formation energy $E_{\mathrm{vac,O}}$ $\left[E_{\mathrm{vac,O,}} = E_{\mathrm{CeO_{2-x(100)}}} + \frac{1}{2}E_{\mathrm{O_2}} - E_{\mathrm{CeO_2(100)}}\right]$ for the $CeO_2(100)$ surface with $c(2\times2)$, $p(2\times2)$ and $c(1\times1)$ periodicity with respect to $\frac{1}{2}E(\mathrm{O_2}) = -4.939$ eV. Molecular $E_{\mathrm{ads,O_2^{x-}}}$ $(x = 0, 1, 2)$ $\left[E_{\mathrm{ads,O_2^{x-}}} = E_{\mathrm{O_2^{x-}/CeO_{2-x}(100)}} - E_{\mathrm{O_2}} - E_{\mathrm{CeO_{2-x}(100)}}\right]$, and net $E_{\mathrm{ads,O}}$ $\left[E_{\mathrm{ads,O,}} = E_{\mathrm{O_2^{x-}/CeO_{2-x}(100)}} - \frac{1}{2}E_{\mathrm{O_2}} - E_{\mathrm{CeO_2(100)}}\right]$ adsorption energies of peroxide ($O_2^{2-}$) and superoxide ($O_2^-$) species at the $CeO_{2\text{-}x}(100)$ surface. Raman shift and Raman intensity for the $O_2^{x-}$ stretching mode and $O_2^{x-}$ bond length. The calculated oxygen vacancy formation energy $E_{\mathrm{vac,O}}$ is in accordance with literature values. [24] [25] The calculations were performed at 400 eV cutoff energy, neglecting van der Waals interactions.

| Structure | Cov. | $E_{\mathrm{tot}}$ [eV] | $E_{\mathrm{vac,O}}$ [eV/$O_{vac}$] | $E_{\mathrm{ads,O_2^{x-}}}$ [eV/$O_2^{x-}$] | $E_{\mathrm{ads,O}}$ [eV/O] | Raman Shift [$cm^{-1}$] | Intensity | Bond length [Å] |
|---|---|---|---|---|---|---|---|---|
| $c(2\times2)$ $O_{vac}$ = 0 | | -959.603 | | | | | | |
| $c(2\times2)$-1 $O_{vac}$ = 1 | | -953.203 | 1.392 | | | | | |
| $c(2\times2)$-2 $O_{vac}$ = 1 | | -953.218 | 1.446 | | | | | |
| $c(2\times2)$-3 $O_{vac}$ = 1 | | -953.190 | 1.473 | | | | | |
| $p(2\times2)$ $O_{vac}$ = 0 | | -479.802 | | | | | | |
| $p(2\times2)$-1 $O_{vac}$ = 1 | | -472.892 | 1.970 | | | | | |
| $p(2\times2)$-2 $O_{vac}$ = 1 | | -472.987 | 1.875 | | | | | |
| $p(2\times2)$-3 $O_{vac}$ = 1 | | -473.038 | 1.824 | | | | | |
| $c(1\times1)$ $O_{vac}$ = 0 | | -239.898 | | | | | | |
| $c(1\times1)$-1 $O_{vac}$ = 1 | | -232.915 | 2.044 | | | | | |
| $c(1\times1)$-2 $O_{vac}$ = 1 | | -232.904 | 2.055 | | | | | |

| | | | | | | | |
|---|---|---|---|---|---|---|---|
| **Peroxide $O_2^{2-}/CeO_{2-x}$(100)** | | | | | | | |
| *c*(2×2) | 0.125 | -964.882 | -1.732 | -0.340 | 868 | 1407 | 1.468 |
| *p*(2×2) | 0.25 | -485.058 | -2.141 | -0.317 | 868 | 1075 | 1.468 |
| *c*(1×1)-1 | 0.5 | -245.160 | -2.367 | -0.323 | 873 | 985 | 1.467 |
| *c*(1×1)-2 | 1.0 | -250.066 | - | -0.145 | 907 | 2637 | 1.455 |
| **Superoxide $O_2^{-}/CeO_{2-x}$(100)** | | | | | | | |
| *c*(2×2) NN | 0.125 | -964.494 | -1.344 | 0.048 | 1050 | 435 | 1.364 |
| *c*(2×2) sub | 0.125 | -964.211 | -1.061 | 0.331 | 1024 | 1120 | 1.374 |
| *c*(2×2) NNN | 0.125 | -964.326 | -1.176 | 0.216 | 1025 | - | 1.374 |
| *c*(2×2) up-1 [a] | 0.125 | -964.148 | -0.996 | 0.394 | 1174 | 233 | 1.334 |
| *c*(2×2) up-2 [a] | 0.125 | -964.072 | -0.922 | 0.471 | 1179 | 640 | 1.340 |
| *p*(2×2) NN | 0.25 | -484.542 | -1.625 | 0.199 | 1046 | 4514 | 1.371 |
| *p*(2×2) sub | 0.25 | -484.296 | -1.379 | 0.445 | 1014 | - | 1.382 |
| *p*(2×2) up-1 [a] | 0.25 | -484.113 | -1.196 | 0.628 | 1192 | 140 | 1.334 |
| *p*(2×2) up-2 [a] | 0.25 | -484.141 | -1.224 | 0.600 | 1188 | 35 | 1.339 |
| *c*(1×1) NN | 0.5 | -244.626 | -1.833 | 0.212 | 1070 | 1232 | 1.366 |
| *c*(1×1) sub | 0.5 | -244.310 | -1.517 | 0.528 | 1045 | - | 1.376 |
| **Molecular $O_2/CeO_2$(100)** | | | | | | | |
| *c*(2×2) | 0.125 | -969.550 | -0.069 | | 1544 | 3270 | 1.233 |
| *p*(2×2) | 0.25 | -489.746 | -0.066 | | 1545 | 4103 | 1.233 |
| *c*(1×2) | 0.5 | -249.837 | -0.060 | | 1550 | 1742 | 1.233 |

[a] one imaginary frequency

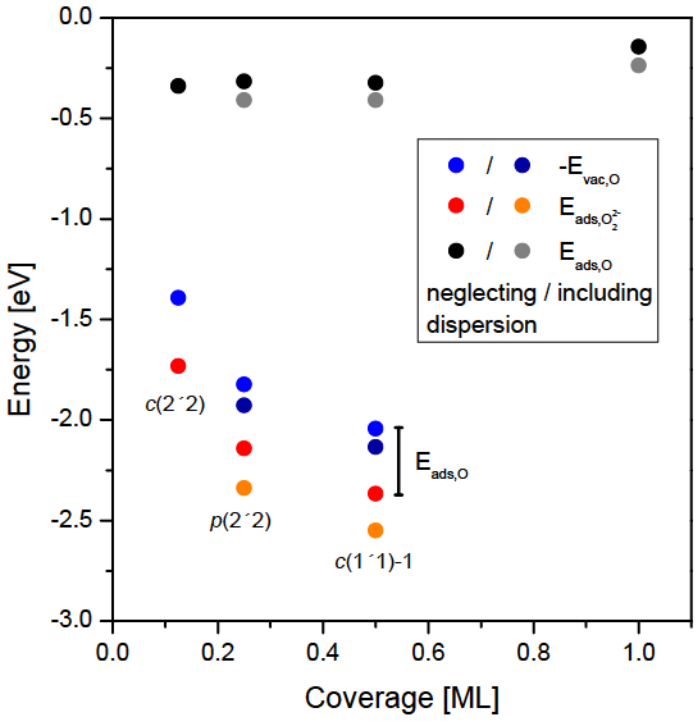


**Figure S11:** Oxygen vacancy healing energies $-E_{\mathrm{vac,O}}$ (blue circles) [eV/O], molecular $E_{\mathrm{ads},O_2^{2-}}$ [eV/ $O_2^{2-}$] (red circles), and net oxygen $E_{\mathrm{ads,O}}$ [eV/O] adsorption energy (black circles) for peroxide species ($O_2^{2-}$) adsorbed at the $CeO_{2-x}$(100) surface as a function of coverage. Dark blue, orange, and grey refers to the corresponding energies including dispersion interactions.

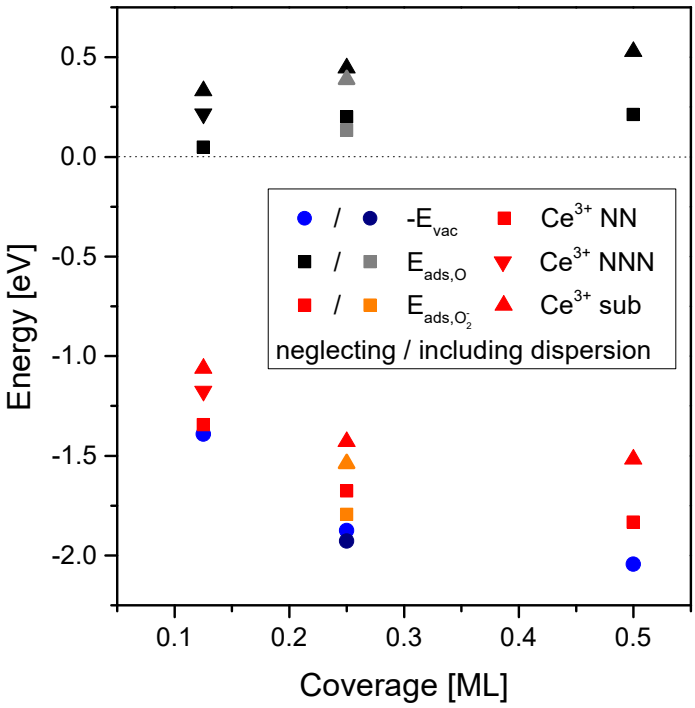


**Figure S12:** Oxygen vacancy healing energies $-E_{\mathrm{vac,O}}$ [eV/O] (blue circles), molecular $E_{\mathrm{ads,O_2^-}}$ [eV/ $O_2^{2-}$] (red symbols), and atomic $E_{\mathrm{ads,O}}$ [eV/O] oxygen adsorption energy (black symbols) of peroxide species ($O_2^-$) adsorbed at the $CeO_{2-x}$(100) surface as a function of coverage. Squares refer to the $Ce^{3+}$ at a nearest neighbor cationic position (NN) to the superoxide, triangle down to the $Ce^{3+}$ at a next nearest neighbor cationic position (NNN) at the surface, and triangle up to a NNN $Ce^{3+}$ in the subsurface. Dark blue, orange, and grey refers to the corresponding energies including dispersion interaction.

## References


1. Filtschew, A.; Hofmann, K.; Hess, C, Ceria and Its Defect Structure: New Insights from a Combined Spectroscopic Approach. *J. Phys. Chem. C* **2016**, *120*, 6694-6703.
2. Mai, H.-X.; Sun, L.-D.; Zhang, Y.-W.; Si, R.; Feng, W.; Zhang, H.-P.; Liu, H.-C.; Yan, C.-H., Shape-Selective Synthesis and Oxygen Storage Behavior of Ceria Nanopolyhedra, Nanorods, and Nanocubes. *J. Phys. Chem. B* **2005,** *109*, 24380-24385.
3. Nottbohm, C. T.; Hess, C., Investigation of Ceria by Combined Raman, UV-Vis and X-ray Photoelectron Spectroscopy. *Catal. Commun.* **2012**, *22*, 39-42.
4. Schilling, C.; Hess, C., Real-Time Observation of the Defect Dynamics in Working Au/$CeO_2$ Catalysts by Combined Operando Raman/UV-Vis Spectroscopy. *J. Phys. Chem. C* **2018**, *122*, 2909-917.
5. Brunauer, S.; Emmett, P. H.; Teller, E., Adsorption of Gases in Multimolecular Layers. *J. Am. Chem. Soc.* **1938**, *60*, 309-319.
6. Filtschew, A.; Stranz, D.; Hess, C., Mechanism of $NO_2$ Storage in Ceria Studied by Combined In Situ Raman/FT-IR Spectroscopy. *Phys. Chem. Chem. Phys.* **2013**, *15*, 9066-9069.
7. Schilling, C.; Hofmann, A.; Hess, C.; Ganduglia-Pirovano, M. V., Raman Spectra of Polycrystalline $CeO_2$: A Density Functional Theory Study. *J. Phys. Chem. C* **2017,** *121*, 20834-20849.
8. Dudarev, S. L.; Botton, G. A.; Savrasov, S. Y.; Humphreys, C. J.; Sutton, A. P., Electron-Energy-Loss Spectra and the Structural Stability of Nickel Oxide: An LSDA+U Study. *Phys. Rev. B: Condens. Matter* **1998**, *57*, 1505-1509.
9. Perdew, J. P.; Burke, K.; Ernzerhof, M., Generalized Gradient Approximation Made Simple. *Phys. Rev. Lett.* **1996**, *77*, 3865-3868.
10. Kresse, G.; Hafner, J., *Ab Initio* Molecular Dynamics for Liquid Metals. *Phys. Rev. B: Condens. Matter* **1993**, *47*, 558-561.
11. Kresse, G.; Hafner, J., *Ab Initio* Molecular-Dynamics Simulation of the Liquid-Metal–Amorphous-Semiconductor Transition in Germanium. *Phys. Rev. B: Condens. Matter* **1994**, *49*, 14251-14269.
12. Kresse, G.; Furthmüller, J., Efficiency of Ab-Initio Total Energy Calculations for Metals and Semiconductors Using a Plane-Wave Basis Set. *Comput. Mater. Sci.* **1996**, *6*, 15-50.

13. Kresse, G.; Furthmüller, J., Efficient Iterative Schemes for *Ab Initio* Total-Energy Calculations Using a Plane-Wave Basis Set. *Phys. Rev. B: Condens. Matter* **1996**, *54*, 11169-11186.
14. Kresse, G.; Joubert, D., From Ultrasoft Pseudopotentials to the Projector Augmented-Wave Method. *Phys. Rev. B: Condens. Matter* **1999**, *59*, 1758-1775.
15. S. Fabris, S. de Gironcoli, S. Baroni, G. Vicario, G. Balducci, Taming Multiple Valency with Density Functionals: A Case Study of Defective Ceria. *Phys. Rev. B: Condens. Matter* **2005**, *71*, 041102.
16. Blöchl, P. E., Projector Augmented-Wave Method. *Phys. Rev. B: Condens. Matter* **1994**, *50*, 17953-17979.
17. Monkhorst, H. J.; Pack, J. D., Special Points for Brillouin-Zone Integrations. *Phys. Rev. B: Condens. Matter* **1976**, *13*, 5188-5192.
18. Grimme, S., Accurate Description of Van Der Waals Complexes by Density Functional Theory Including Empirical Corrections. *J. Comput. Chem.* **2004**, *25*, 1463-1473.
19. Grimme, S., Semiempirical GGA-Type Density Functional Constructed with a Long-Range Dispersion Correction. *J. Comput. Chem.* **2006**, *27*, 1787-1799.
20. C. Penschke, J. Paier, J. Sauer, Oligomeric Vanadium Oxide Species Supported on the $CeO_2$(111) Surface: Structure and Reactivity Studied by Density Functional Theory. *J. Phys. Chem. C* **2013**, *117*, 5274-5285.
21. Baroni, S.; de Gironcoli, S.; Dal Corso, A.; Giannozzi, P., Phonons and Related Crystal Properties from Density-Functional Perturbation Theory. *Rev. Mod. Phys.* **2001**, *73*, 515-562.
22. Gajdoš, M.; Hummer, K.; Kresse, G.; Furthmüller, J.; Bechstedt, F., Linear Optical Properties in the Projector-Augmented Wave Methodology. *Phys. Rev. B: Condens. Matter* **2006**, *73*, 045112.
23. Porezag, D.; Pederson, M. R., Infrared Intensities and Raman-Scattering Activities within Density-Functional Theory. *Phys. Rev. B: Condens. Matter* **1996**, *54*, 7830-7836.
24. Kropp, T.; Paier, J., Activity versus Selectivity of the Methanol Oxidation at Ceria Surfaces: A Comparative First-Principles Study. *J. Phys. Chem. C* **2015**, *119*, 23021-23031.
25. Yang, C.; Yu, X.; Heißler, S.; Weidler, P. G.; Nefedov, A.; Wang, Y.; Wöll, C.; Kropp, T.; Paier, J.; Sauer, J., $O_2$ Activation on Ceria Catalysts - The Importance of Substrate Crystallographic Orientation. *Angew. Chem. Int. Ed.* **2017,** *56*, 16399-16404.